Chapter-3

Preparation of Graphitic Carbon Like Material from ARA Fractions of Vacuum Residue

3.1 Introduction

Graphite, a crystalline allotrope of carbon with a distinctive layered arrangement, has established itself as an essential material across numerous technological domains, including metallurgy, nuclear engineering, energy storage, and high-temperature applications. It can be obtained naturally from geological deposits or produced synthetically via industrial processing. Its unique anisotropic structure, superior electrical conductivity, and thermal stability account for its widespread adoption in advanced materials and energy technologies.

Among the petroleum refining streams, vacuum residue (VR)—a heavy, asphaltene-rich fraction obtained from the vacuum distillation of atmospheric residue—provides a carbon-dense, aromatic precursor pool rich in polycyclic aromatic hydrocarbons (PAHs), resins, and asphaltenes, albeit with elevated heteroatoms (S, N, and metals). This makes VR an attractive feedstock for conversion into pitch, needle coke, and ultimately synthetic graphite [1]. Owing to its high aromaticity and ability to form liquid-crystalline (mesophase) domains during thermal polycondensation, VR enables controlled microtexture development during carbonization, which is crucial for producing high-performance graphitic carbons applied in anodes, bulk graphite blocks, and specialty refractories [1–3].

Two principal industrial routes exist for transforming VR into graphitizable intermediates. The first involves direct thermal treatment or modification of VR into mesophase pitch. Under carefully controlled thermal conditions (typically 400–500 °C in an inert atmosphere) and pre-modifications such as oxidative/nitrative treatments or solvent fractionation, VR can be converted into optically anisotropic mesophase pitches with low quinoline-insoluble (QI) content, suitable for spinning or molding [2–4]. Liu et al. demonstrated that naphthenic VR, after targeted modification, produces high-quality mesophase pitch through single-stage thermal treatment, establishing key structure–processing correlations such as softening point, toluene/quinoline solubility, and

mesophase content that dictate coke and graphite performance [2]. Likewise, Yamada et al. showed as early as 1975 that petroleum-derived VR could be systematically heat-treated to yield binder pitches with tunable rheology and coking values, laying the foundation for today's VR-based graphite block manufacturing [3]. More recent refinements have enabled VR/petroleum fraction oil (PFO)-derived binder pitches that facilitate low-temperature forming while delivering high coking values, producing graphite blocks with reduced porosity and enhanced compressive strength after graphitization at 2700 °C [4].

The second pathway is delayed coking of VR, which yields anisotropic (needle) coke characterized by highly oriented flow textures and a low coefficient of thermal expansion (CTE)—properties critical for high-performance graphite electrodes and specialty carbons. Here, the interplay of feedstock chemistry (e.g., sulfur, metals, and Conradson carbon content), recycle oil addition, and coking drum conditions determines mesophase development, anisotropy, and the suppression of undesirable shot coke [5–7]. Pilot- and commercial-scale studies have established clear process–structure relationships, showing how VR composition and coker severity govern the transition from mosaic to flow textures, which in turn dictates the graphitizability and performance of the resulting synthetic graphite [6–7].

Across both approaches, microtexture control—encompassing mesophase domain size, orientation, and impurity management—remains pivotal. Advances in characterization techniques, such as in-situ optical texture analysis of heavy-oil coking, now provide real-time feedback on mesogen evolution, thereby accelerating optimization of VR chemistry, processing conditions, and mesophase anisotropy [8]. When appropriately purified, with QI content minimized and graphitization temperatures ≥2700–3000 °C applied, VR-derived graphites have been shown to match or even surpass commercial benchmarks in applications such as lithium-ion battery anodes and dense graphite blocks [2–4,9]. This chapter therefore concentrates on (i) VR chemistry and pretreatment strategies, (ii) mesophase pitch synthesis and structure–property relationships, (iii) delayed coking of VR to needle coke, (iv) pitch design for dense graphite blocks, and (v) correlations between macrotexture/impurities and the electrochemical and thermo-mechanical performance of synthetic graphite [10].

3.1.1. Distinguishing Synthetic from Natural Graphite: A Foundational Comparison

Synthetic graphite is an engineered industrial material derived from carbon-rich feedstocks such as petroleum coke, coal tar pitch, or other high-carbon precursors, which are subjected to graphitization at temperatures exceeding 2500–3000 °C [11]. Unlike natural graphite, whose properties are constrained by geological variability, synthetic graphite reflects the precision of industrial design. This controlled synthesis ensures reproducible and tunable characteristics, making synthetic graphite highly suitable for advanced technological applications where consistency is paramount [12].

A key advantage of synthetic graphite lies in its superior purity. Industrial processes enable extensive removal of metallic and non-metallic impurities, yielding materials that can surpass 99.9 wt% carbon [13]. For electrochemically sensitive applications such as lithium-ion battery anodes, purity requirements are even more stringent, with levels exceeding 99.95% to ensure stability and long cycle life [14]. By contrast, natural graphite exhibits considerable variability in carbon content depending on deposit type and geological origin, with flake graphite typically ranging from 80% to 98% purity [15]. This inconsistency necessitates extensive beneficiation, often involving flotation, acid leaching, or thermal purification, which increases production costs and may lead to yield losses [16].

Structural features further differentiate synthetic from natural graphite. Synthetic graphite, formed under controlled graphitization, generally exhibits a uniform microstructure with consistent crystallite alignment, providing predictable electrical and mechanical performance [17]. Natural graphite, however, shows heterogeneity in crystallite size, orientation, and defect density, reflecting the variability of its geological formation [18]. Although certain high-grade natural graphite deposits produce large crystallites that enhance conductivity, the lack of structural uniformity and reproducibility often undermines these benefits [19]. Consequently, in advanced engineering contexts such as energy storage or high-temperature metallurgy, the uniformity of synthetic graphite is more valuable than the occasional superior performance of natural grades [20].

Density comparisons also reveal important contrasts. The theoretical density of an ideal graphite crystal with a fully ordered hexagonal lattice is 2.26 g/cm³ [21]. Natural graphite often falls below this value (1.48–2.23 g/cm³) due to porosity, structural imperfections, and impurities [22]. Synthetic graphite, owing to its higher purity and optimized processing, typically achieves bulk densities of 1.6–1.9 g/cm³ [23]. However, some forms—such as synthetic powders or expanded graphite—can display lower densities and higher porosities than natural flake graphite, underscoring that density is not an absolute differentiator but depends on processing, feedstock, and application [24].

Ultimately, the selection between natural and synthetic graphite depends on the balance of performance, cost, and consistency. Natural graphite remains dominant in cost-sensitive applications such as refractories and lubricants, while synthetic graphite prevails in high-performance sectors—including electric arc furnace electrodes, lithium-ion batteries, and nuclear reactors—where uniformity, purity, and reliability are essential [25].

3.1.2. Vacuum Residue as a Precursor Material

3.1.2.1 Characterization of Vacuum Residue: Compositional and Structural Profile

Vacuum residue (VR) represents the non-volatile, high-boiling fraction that remains after vacuum distillation of crude oil, following the separation of lighter, more valuable hydrocarbons such as naphtha, kerosene, and gas oils [26]. Traditionally regarded as a low-value by-product in the refining chain, VR has more recently attracted attention in advanced materials science due to its high carbon content and strongly aromatic character, which together render it a promising feedstock for synthetic graphite production [27]. However, this potential is counterbalanced by the material's inherent complexity and high impurity load, which create challenges for both processing and end-use applications [28].

Physically, VR is a viscous, black-to-dark-brown material with a strong asphaltic odour [29]. Its macromolecular characteristics are dominated by heavy polyaromatic structures, with a wide molecular weight distribution typically ranging between 1170 and 3920 Da [30]. Elemental analysis consistently highlights its carbon-rich composition, with carbon content between 88.7% and 90% by weight [31]. However, heteroatoms are also abundant:

oxygen is present in the range of 5.7–15.8 wt%, while sulphur generally accounts for 1.4–3.5 wt% [31]. In addition, VR is heavily metal-laden, with vanadium contributing up to 64.3% of the total metallic fraction and nickel accounting for as much as 62.5% [30]. These impurities, especially the transition metals, play a detrimental role during high-temperature treatment, as they catalyse undesirable side reactions and can interfere with graphitization [32].

From a structural perspective, VR is a complex mixture of saturates, aromatics, resins, and asphaltenes (SARA fractions) [33]. Among these, the asphaltene fraction is particularly problematic for carbon material synthesis. Asphaltenes are defined by their polyaromatic, highly cross-linked structures that are "pinned" by heteroatoms and metals, severely hindering molecular mobility and plastic flow during pyrolysis [26]. This, in turn, disrupts mesophase formation — a critical precursor stage for producing high-quality graphitizable carbon [34].

A consolidated summary of the principal physicochemical properties of raw vacuum residue is presented in Table 3.1, providing a baseline for evaluating both its potential advantages and limitations as a synthetic graphite precursor.

Property	Value	References
Carbon Content	88.7–90 wt%	[31]
Oxygen Content	5.7–15.8 wt%	[31]
Sulfur Content	1.4–3.5 wt%	[31]
Asphaltene Content	~13.3 wt%	[35]
Vanadium Content	64.3% of total metal fraction	[30]
Nickel Content	62.5% of total metal fraction	[30]
Physical State	Viscous, asphalt-like liquid	[29]
Molecular Weight Range	1170–3920 Da	[30]

Table 3.1: Key Properties of Raw Vacuum Residue (VR)

3.1.2.2 The Economic and Aromatic Advantage of a Low-Value Feedstock

The principal motivation for utilizing vacuum residue (VR) as a precursor for synthetic graphite lies in its economic viability. As a byproduct of vacuum distillation, VR is often categorized as a low-value waste stream in petroleum refining. Its abundant availability and comparatively low cost provide a compelling financial incentive for its valorization into high-demand, high-value products such as synthetic graphite [18]. This economic advantage strongly underpins the development of advanced processing technologies designed to convert VR into graphitizable intermediates, despite the technical complexities associated with its transformation.

In addition to its economic merit, VR possesses a structural feature that renders it particularly suitable for graphite precursor applications—its high aromatic content [18]. Aromatic hydrocarbons, defined by their ring-shaped molecular structures, are critical building blocks for mesophase pitch formation. Mesophase pitch represents a liquid-crystalline intermediate that is essential for the subsequent transformation into the ordered hexagonal ring structures characteristic of crystalline graphite [2].

Thus, VR embodies a duality: while its high carbon and aromatic content make it a promising raw material, its significant impurity load and asphaltenic composition present formidable challenges. Overcoming these constraints requires sophisticated chemical and thermal engineering strategies. The result is a transformative process that elevates an otherwise low-value refinery byproduct into a strategically important industrial material with wide-ranging applications.

3.1.3. The Multi-Stage Manufacturing Process

The production of high-purity synthetic graphite from vacuum residue (VR) is inherently complex, reflecting the need to systematically address the feedstock's structural and compositional limitations. Unlike naturally occurring graphite, which is directly mined, and beneficiated, synthetic graphite must be engineered through a sequence of thermal and chemical transformations. This process is designed to progressively convert VR, a "hard" carbon precursor characterized by disordered, cross-linked aromatic structures, into a

highly crystalline “soft” carbon product with the long-range order characteristic of graphite [2].

At its core, the manufacturing route consists of several interdependent stages. First, pretreatment steps—including de-metallization, solvent fractionation, or oxidative modification—are often employed to reduce heteroatom and metal impurities and to enhance the molecular mobility of asphaltenes. This improves the precursor’s suitability for mesophase development. Next, controlled thermal polymerization is applied to induce the formation of mesophase pitch, a liquid-crystalline intermediate phase in which polyaromatic molecules align into anisotropic domains. The quality of mesophase—defined by parameters such as optical anisotropy, softening point, and quinoline insoluble (QI) content—directly governs downstream performance.

Following pitch synthesis, carbonization is carried out under inert atmospheres at elevated temperatures (typically 600–1200 °C). In this stage, non-carbon elements such as hydrogen, oxygen, nitrogen, and sulfur are progressively eliminated, while the aligned aromatic structures begin to consolidate into more ordered macrotextures. The final and most critical stage is graphitization, conducted at temperatures exceeding 2500–3000 °C, where the turbo static carbon layers undergo rearrangement into a highly ordered hexagonal lattice. This transformation imparts the essential characteristics of synthetic graphite, including high electrical conductivity, thermal stability, and mechanical integrity.

The multi-stage pathway is therefore both a technical necessity and a strategic opportunity: each stage enables refinement of structure and composition, thereby overcoming the challenges posed by VR’s high impurity load and complex molecular architecture. The result is a material that not only matches but can, under optimized conditions, surpass natural graphite in performance for demanding industrial applications [2].

3.1.4 Precursor Upgrading: The Critical First Step to Mitigate Impurities

The initial and arguably most critical stage in the conversion of vacuum residue (VR) to synthetic graphite is precursor upgrading. Asphaltenes and other highly cross-linked polyaromatic structures present in VR render it a “hard” carbon material, meaning it resists

ordering and will not readily undergo graphitization [2]. This structural rigidity stems from the limited molecular mobility of asphaltenes, whose strongly fused aromatic rings are constrained by heteroatoms and metal complexes.

For successful graphitization, the carbon precursor must be capable of passing through a fluid, liquid-crystalline mesophase state during heat treatment. The mesophase serves as a transitional medium in which pre-graphitic aromatic structures achieve alignment and orientation prior to the high-temperature graphitization stage. Without this intermediate alignment, the carbon matrix remains disordered, preventing the development of the highly crystalline lattice essential for synthetic graphite's desirable properties [2].

Precursor upgrading is therefore indispensable, as it alters the structure and composition of VR to improve its ability to form mesophase. This is typically achieved through strategies such as solvent fractionation, oxidative modification, hydrodemetallization, or selective hydrogenation, each of which reduces impurity levels and enhances molecular fluidity. By mitigating the negative influence of asphaltenes and transition metals, upgrading transforms VR from an intractable hard carbon into a viable feedstock for downstream mesophase pitch synthesis, carbonization, and ultimately graphitization [2].

3.1.5 Impurity Removal: Desulfurization, Dementalization, and Asphaltene Cracking

One of the principal challenges in converting vacuum residue (VR) into synthetic graphite is its exceptionally high impurity content. Contaminants such as sulfur and transition metals—particularly vanadium and nickel—are present in significant concentrations. These species not only poison catalysts employed in downstream upgrading and refining operations but also negatively affect the structural integrity and electrochemical properties of the final graphite product [22]. As such, impurity reduction represents a critical pre-treatment requirement in the multi-stage manufacturing pathway.

Conventional impurity management strategies rely heavily on catalytic hydrotreating, which facilitates hydrodemetallization (HDM) and hydrodesulfurization (HDS). In these processes, transition-metal catalysts promote hydrogenation reactions that remove metals

and sulfur compounds from the VR matrix, thereby improving its suitability for mesophase formation and subsequent graphitization [23]. While effective, these methods are resource- and energy-intensive, highlighting the need for innovative alternatives.

Recent research has explored advanced technologies, such as microwave-assisted catalytic cracking, which employs carbon-based susceptors in combination with metal nanoparticles to enhance the breakdown of large asphaltene molecules. This technique not only reduces asphaltene content but also significantly lowers the viscosity of VR, improving its processability and mesophase-forming potential [19]. Such approaches represent promising pathways toward more efficient and sustainable precursor upgrading, enabling the valorization of VR into high-purity synthetic graphite.

3.1.6 Mesophase Pitch Formation: The Indispensable Liquid-Crystalline State

Following impurity reduction and precursor upgrading, the next essential stage in the conversion of vacuum residue (VR) to synthetic graphite is the formation of mesophase pitch (MP). This process is typically achieved through controlled co-pyrolysis, during which the aromatic compounds present in VR undergo polymerization to form the liquid-crystalline domains necessary for subsequent graphitization [18]. The mesophase state is indispensable, as it provides the molecular mobility and structural alignment required for the transformation of disordered hydrocarbons into ordered graphitic lattices.

The efficiency of mesophase pitch formation can be significantly enhanced by the addition of suitable organic modifiers. Compounds such as gum rosin and dehydrated castor oil (DCO) have been demonstrated to promote mesophase development due to their conjugated double bonds and free radical activity [18]. These additives facilitate polymerization and improve the thermal stability of the pitch, thereby enhancing its capacity to form graphitizable structures at elevated temperatures.

Experimental studies have shown that incorporating gum rosin into VR during co-pyrolysis at 450 °C for 120 minutes can reduce the precursor's C/H molar ratio from 2.43 to 2.01, a transformation that directly favors the growth of well-ordered graphite crystallites [18]. In addition, this modification has been reported to significantly improve the porosity of the

resulting carbon material, increasing its surface area from 120.81 m^2/g to 462.19 m^2/g [18]. Such findings underscore the dual role of mesophase pitch formation: not only does it establish the structural foundation for graphitization, but it also tailors the physicochemical properties of the carbon product for advanced functional applications.

3.1.7 Carbonization: Transforming the Precursor to Amorphous Carbon

Following mesophase pitch formation, the material undergoes carbonization, a critical intermediate step in synthetic graphite production. Carbonization typically involves heating the precursor to temperatures ranging between 500 °C and 1200 °C in an oxygen-free environment, thereby preventing combustion and promoting structural transformation [7]. During this process, volatile components—including hydrogen, oxygen, and nitrogen—are expelled as gaseous byproducts, while the solid residue becomes progressively enriched in carbon. The product of carbonization is a highly carbonaceous but still largely amorphous material, which serves as the essential foundation for subsequent graphitization [7,18].

Experimental studies provide concrete examples of this step. For instance, heating an upgraded precursor to 700 °C for 120 minutes under nitrogen flow has been shown to effectively remove heteroatoms while preserving the aligned domains formed during mesophase development [18]. This controlled elimination of volatile species not only enhances the purity of the material but also improves its structural readiness for the final, high-temperature transformation into crystalline graphite.

3.1.8 Graphitization: The High-Temperature Leap to a Crystalline Lattice

Graphitization represents the defining stage of synthetic graphite production, where the disordered carbon structure is transformed into a highly ordered, crystalline lattice. This process is both a thermodynamic and kinetic challenge, requiring carefully controlled conditions to achieve structural perfection [26]. Typically, graphitization is carried out at temperatures between 2300 °C and 3000 °C, which provide the necessary atomic mobility

for carbon atoms to rearrange into the stable, three-dimensional hexagonal lattice of graphite [2].

The operation is conducted in specialized graphitization furnaces, often under vacuum or inert gas atmospheres, to suppress oxidative degradation at such extreme temperatures [26]. Despite its central importance, the step is highly energy-intensive, motivating extensive research into methods that lower the thermal burden while maintaining high crystallinity. One promising approach involves the use of heteroatom additives such as boron, phosphorus, or nitrogen, which act as graphitization catalysts and accelerate lattice ordering [31].

For instance, the incorporation of boric acid into a pitch-derived precursor has been shown to substantially improve crystallinity. At a treatment temperature of 2500 °C, the doped material achieved a graphitization ratio of 97.24% with an interlayer spacing (d (002)) of 3.355 Å, a value nearly identical to the theoretical graphite spacing of 3.353 Å. By contrast, the undoped sample under the same conditions reached only 76.5% crystallinity, underscoring the catalytic role of boron in lowering the energetic barrier to structural ordering [31].

Thus, graphitization not only defines the microstructural quality of synthetic graphite but also represents the critical stage where process innovation and energy efficiency intersect, shaping both the performance of the material and the economics of large-scale production.

3.1.9 Post-Processing and Refinement

The final stages of synthetic graphite production focus on post-processing and refinement, which are essential for tailoring the material to specific industrial applications. Depending on the end use, the bulk graphite may undergo mechanical processing such as grinding, milling, or shaping into powder, blocks, or electrodes [3]. These steps ensure that the physical form of the product matches the requirements of applications ranging from metallurgical operations to advanced electrochemical devices.

For high-purity applications, such as lithium-ion batteries and nuclear technologies, additional purification is often required. In such cases, thermal purification is commonly employed, in which the graphite is heated to temperatures above 2800 °C to volatilize residual metallic and non-metallic contaminants [6]. Alternatively, chemical purification methods may be used, where strong acids are applied to dissolve impurities that are otherwise resistant to volatilization [6].

Through these targeted refinement processes, synthetic graphite can be engineered to achieve the precise purity, morphology, and structural characteristics necessary for optimal performance in its diverse range of technological applications.

3.1.10 Properties and Performance of Synthetic Graphite

The multi-stage conversion of vacuum residue into synthetic graphite yields a high-performance material with a distinct set of properties that differentiate it from natural graphite. Unlike its natural counterpart, synthetic graphite can be engineered through controlled manufacturing processes to possess customized characteristics, making it highly attractive for technologically demanding applications.

3.1.11 Crystallinity and Structural Uniformity

One of the primary performance advantages of synthetic graphite lies in its structural uniformity and high crystallinity [7]. During graphitization, carbon atoms are rearranged into a hexagonal lattice, creating a highly ordered structure. The degree of crystallinity can be quantitatively assessed by the interlayer distance (d(002)) between carbon planes. The theoretical spacing for graphite is 3.35 Å, and the closer the measured value is to this standard, the higher the crystallinity [18]. For instance, studies on pitch-based graphite doped with boron have demonstrated a d(002) spacing of 3.355 Å, reflecting near-perfect crystallinity [31]. This high degree of order translates into consistent and predictable performance, which is crucial for advanced applications such as high-performance batteries and electronic devices.

3.1.12 Physical Properties: Density, Porosity, and Thermal Conductivity

The physical properties of synthetic graphite—including density, porosity, and thermal conductivity—are strongly influenced by its engineered production pathway. While the theoretical density of graphite is 2.26 g/cm³ [9], the bulk density of synthetic graphite products typically falls within the range of 1.6–1.9 g/cm³ [11]. Synthetic graphite is also characterized by a relatively high porosity compared to natural graphite [5]. Although high porosity can be a limitation in refractory applications [1], it is advantageous in other contexts. For example, porous synthetic graphite grades offer large surface areas, which are highly desirable for filtration and energy storage technologies [33].

Thermal conductivity represents another key property. Natural graphite generally exhibits superior conductivity due to its larger crystallite sizes [8]. However, synthetic graphite can be tailored during processing to meet specific thermal requirements, such as those encountered in high-temperature furnace applications [7]. This tunability makes it more versatile than natural graphite in contexts where precise thermal management is critical.

3.1.13 Electrical Properties and Chemical Stability

The layered lattice structure of synthetic graphite facilitates the movement of delocalized electrons, thereby providing excellent electrical conductivity [7]. This property is central to its use in electrodes, electrical contacts, and energy storage devices, particularly lithium-ion batteries. In addition to electrical conductivity, synthetic graphite exhibits high chemical stability and resistance to corrosion, even at elevated temperatures [1]. These features make it suitable for harsh industrial environments, where reliability and durability are paramount.

Overall, the combination of engineered crystallinity, tunable physical properties, and robust chemical stability underscores the defining advantage of synthetic graphite. Unlike natural graphite, which is constrained by geological variability, synthetic graphite offers bespoke and reproducible properties that justify its higher cost in high-efficiency, performance-driven markets.

3.1.13.1 High-Value Applications of Synthetic Graphite

The tailored properties of synthetic graphite make it an indispensable material for a wide range of modern technologies. Its applications span from energy storage and metallurgy to advanced industrial and high-temperature environments.

3.1.13.2 Lithium-ion Batteries: The Anode Material of the Electrification Revolution

The single largest and fastest-growing application for synthetic graphite is in the production of lithium-ion batteries [35]. The rechargeable battery sector is projected to account for a dominant market share, with reports indicating it captures more than 39.1% of the global synthetic graphite market [35].

3.1.13.3 The Anode's Role in Battery Performance

Graphite serves as the primary host material for lithium ions in the battery's anode. The layered structure of graphite allows for the reversible intercalation and de-intercalation of lithium ions, which is the fundamental mechanism that enables the battery to store and release energy during charging and discharging cycles [34]. Synthetic graphite is particularly valued for its contribution to the longevity and fast-charging capabilities of modern energy storage devices, which are critical for electric vehicles (EVs) and grid-scale storage systems [4].

3.1.13.4 Specific Purity and Performance Requirements for Battery-Grade Graphite

The high stakes of battery performance and safety necessitate extremely stringent requirements for the anode material. The carbon chemical purity of battery-grade graphite must be better than 99% [38], with some specifications requiring purity to exceed 99.95% to ensure a long cycle life and prevent irreversible reactions that could degrade the battery's performance [6]. Impurities above 500 ppm can be detrimental, as they can lead to the formation of compounds like lithium oxide, which impacts the cell's lifespan [6].

A summary of the specified properties for battery-grade graphite is provided in Table 3.2, highlighting the rigorous standards to which the material must conform. The ability to meet these exact specifications is a key factor in synthetic graphite's dominance in this market.

Property	Value	Source
Purity	>99% [38] to >99.95% [6]	[6], [38]
Ash Content	<0.2%	[39]
Fe Content	<50 ppm	[39]
True Density	2.22–2.26 g/cm³	[39]
First Discharge Capacity	>360 mAh/g	[39]

Table 3.2. Specified Properties of Battery-Grade Graphite

3.1.14 Metallurgical Applications: From Electrodes to Recarburization

Synthetic graphite is a cornerstone material in metallurgy, particularly in electric arc furnace (EAF) steelmaking, where it is used to produce high-purity electrodes. These electrodes are preferred due to their exceptional thermal conductivity**,** resistance to thermal shock**,** and ability to endure extreme operational currents—properties essential for modern steel recycling and smelting operations. In addition to electrodes, synthetic graphite is also a key recarburization agent**.** It's used to finely adjust carbon content in molten iron and steel, enhancing material properties like hardness and strength. Its high purity ensures consistent performance and avoids introducing unwanted impurities during alloy refinement [34].

3.1.15 High-Temperature and Refractory Materials

Synthetic graphite excels in high-temperature refractory applications due to its thermal stability and conductivity. It is utilized in furnace linings, heating elements, and high-temperature reactor insulation thanks to its ability to dissipate heat efficiently and resist thermal shock. Its low thermal expansion coefficient ensures structural integrity under rapid temperature cycling and prolonged high-temperature exposure [7].

3.1.16 Other Advanced Industrial Applications

Synthetic graphite's specialty uses span high-tech industries due to its engineered purity and properties:

- **Semiconductor & Electronics**: High-purity grades are employed in silicon wafer production and thermal management for processors.
- **Nuclear Reactors**: Synthetic graphite serves as a neutron moderator and reflector component. Its effectiveness depends on ultra-pure, impurity-free feed material to avoid compromising reactor
- **Solid Lubricants**: Its layered structure grants excellent lubricity, making it ideal for industrial sliding applications where conventional lubricants fail.
- **Additive Manufacturing & Filters**: Synthetic graphite blocks and powders are also used in specialized moulds, filtration systems, and components for photovoltaic and solar-energy industries

3.1.17 Market, Economic, and Environmental Dynamics

3.1.17.1 The Global Market for Synthetic Graphite and Economic Drivers

The global synthetic graphite market is a rapidly expanding sector, projected to reach USD 13.1 billion by 2034, with a compound annual growth rate (CAGR) of 6.3% [35,42]. This expansion is overwhelmingly driven by the surging demand for high-performance lithium-ion batteries, particularly in the electric vehicle (EV) market [4,44]. The ongoing electrification of transportation and the global shift toward renewable energy integration have positioned synthetic graphite as a strategic material for the energy transition [43].

Asia dominates this market, with China accounting for more than 80% of global synthetic graphite production [40,42]. This concentration creates supply-chain vulnerabilities for other regions, especially considering geopolitical tensions, export controls, and raw material restrictions [35,44]. Moreover, the industry’s reliance on high-grade petroleum feedstocks (such as needle coke) introduces additional challenges, as these resources are both limited and in competition with other industrial sectors [4,45].

3.1.17.2 The Energetic and Environmental Footprint of Production

Synthetic graphite production is among the most energy-intensive carbon material processes, with the Acheson graphitization method often requiring temperatures exceeding 2800–3000 °C and lasting for several weeks [3,4]. This reliance on fossil-fuel-based electricity results in substantial greenhouse gas (GHG) emissions [42].

The literature presents conflicting data regarding the carbon intensity of synthetic graphite. Some studies indicate that synthetic graphite is four times more carbon-intensive than natural graphite anodes [3], while others quantify its footprint at approximately 4.9 kg CO_2 per 1 kg of graphite produced [6]. Interestingly, this figure is comparable to certain natural graphite extraction pathways, suggesting that methodological inconsistencies (e.g., whether to include fossil feedstock carbon) may explain the discrepancies [6,46].

To contextualize this debate, recent lifecycle assessments (LCAs) emphasize that synthetic graphite's footprint depends heavily on energy source (coal vs. hydropower) and process technology [46]. Table 3.3 summarizes the available data.

Production Method	CO_2 Emissions (kg CO_2/kg graphite)	References
Synthetic Graphite	~4.9	6
Natural Graphite	~4.9	6
Natural Graphite (Hydropower)	~1.8	6
Recycled Graphite (Hydro/Pyrometallurgy)	0.53–9.76	42,46

Table 3.3: Environmental Impact Comparison of Graphite Production

3.1.17.3 Pathways to Sustainability: Recycling and Future Precursors

The dual challenge of rising demand and environmental impact has driven significant research into sustainable synthetic graphite pathways. One of the most promising approaches is the recycling of graphite from spent lithium-ion batteries (LIBs). While early recycling efforts emphasized high-value transition metals like nickel and cobalt, recent

studies highlight graphite recovery through hydrometallurgical and pyrometallurgical techniques [43,47]. However, such processes may reduce the crystallinity or graphitization degree of the recycled graphite, limiting its direct reuse in high-performance applications [43].

Another major research frontier is the development of non-fossil precursors for synthetic graphite. Experimental studies report the conversion of biochar derived from biomass (e.g., palm kernel shells, wood, agricultural residues) into battery-grade graphite [45,48]. These renewable pathways not only diversify the supply chain but also offer a substantially reduced carbon footprint, especially when powered by renewable electricity [48]. Such innovations represent critical steps toward building a circular and sustainable graphite economy, aligned with global carbon neutrality goals.

3.2 Materials & Methods

Aromatic, resin and asphaltene (ARA) fractions from three different vacuum residues (Light Crude oil, Heavy Crude oil and Extra Heavy Crude oil) were used as a raw material for preparation of green coke for this study. The raw materials were pyrolyzed at 500°C for 10 min under inert atmospheric conditions as per ASTM D4530 resulting in the formation of green carbon. The obtained green carbon samples were further heat treated in two steps, followed by heating at 900°C with heating rate of 10°C and 1350°C with rate of 5°C and held for 30 min and 5 hr respectively to produce calcined carbon. This was done to remove all volatile matters for further processing to get graphitized carbon. Graphitization was done at 2800°C with heating rate of 15°C and held for 2 hr.

3.2.1 Carbon Residue (ASTM D4530)

Carbon residue is a critical parameter in petroleum analysis, providing insight into the tendency of a fuel or crude oil to form coke-like deposits when subjected to high temperatures (Asemani et al., 2020). ASTM D4530, the Micro Carbon Residue (MCR) Test as shown in fig 2.4, is a widely used method to determine the carbon residue content of petroleum products, heavy oils, and vacuum residues (Nazar et al., 2008). This method helps in refining processes, catalyst selection, and fuel quality assessment.

Figure 3.4: Carbon Residue test apparatus

Principle of ASTM D4530

The Micro Carbon Residue (MCR) test involves heating a weighted petroleum sample in a controlled oxygen-free environment, causing thermal decomposition. The volatile components evaporate, leaving behind a carbonaceous residue. The weight of this residue is then measured and expressed as a percentage of the original sample.

Key Reaction Steps:

1. Sample Preparation – The sample is pre-weighed and placed in a quartz crucible inside a controlled furnace.
2. Heating in an Inert Atmosphere – The sample undergoes pyrolysis at temperatures up to 500-600°C in an oxygen-free environment (typically nitrogen).
3. Evaporation of Volatiles – Lighter hydrocarbons and volatile matter are driven off.
4. Coking Process – The remaining heavy hydrocarbons decompose, forming a solid carbonaceous residue.
5. Final Residue Weighing – The percentage of carbon residue is calculated based on weight loss.

The formula for calculating carbon residue is:

$$\%\text{Carbon Residue} = \left(\frac{\text{Final Residue Weight}}{\text{Initial Sample Weight}}\right) \times 100$$

- Indicates fuel stability and coking tendency.
- Higher carbon residue suggests a higher tendency to form deposits in engines and refining processes.

Petroleum Product	**Carbon Residue (%)**	**Significance**
Light Fuel Oils	< 0.1%	Low deposit formation, clean burning
Heavy Fuel Oils	2 – 10%	Higher coke formation used in boilers
Vacuum Residues	10 – 25%	Feedstock for bitumen and heavy oil processing
Asphaltenes	> 25%	High tendency to form coke in cracking units

Table 2.4: Typical Carbon Residue Values for Different Petroleum Products (Sarowha, S.L.S., 2005)

ASTM D4530 method was used for the determination of the amount of carbon residue in ARA fraction.

3.2.2 Elemental Analysis (CHNSO)

Elemental analysis of Carbon (C), Hydrogen (H), Nitrogen (N), Sulfur (S), and Oxygen (O) (CHNSO) is a fundamental technique used to determine the composition of petroleum products, polymers, pharmaceuticals, and environmental samples. This analysis provides

insight into the chemical composition, purity, and stability of materials, helping in quality control and formulation studies (Azam et al., 2021).

Figure 2.5: Instrumentation of Elemental Analysis

Principle of CHNSO Analysis

CHNSO analysis is based on high-temperature combustion of a sample, converting its elements into gases that can be quantified using detectors. The method follows ASTM D5291 (for CHN), ASTM D3176 (for ultimate analysis of coal and coke), and ASTM D4239 (for sulfur analysis).

Basic Reactions in CHNSO Analysis

- Carbon (C) → CO_2 (Carbon Dioxide)
- Hydrogen (H) → H_2O (Water Vapor)
- Nitrogen (N) → N_2 or NO_x (Oxides of Nitrogen)
- Sulfur (S) → SO_2 (Sulfur Dioxide)
- Oxygen (O) → CO or CO_2 (Carbon Monoxide/Dioxide, by difference method)

Equipment	**Function**
Elemental Analyzer (e.g., CHNSO Analyzer)	Performs combustion and detection of gases

Furnace (1100-1400°C)	Oxidizes the sample into gas form
Oxygen Supply	Ensures complete combustion
TCD Detector (Thermal Conductivity Detector)	Measures carbon, hydrogen, and nitrogen
Infrared (IR) Detector	Detects sulfur and oxygen

Table 3.4: Equipment and Materials Required (Prado et al., 2017)

In this study, the CHNSO content was determined using the Elementary Vario Macro CUBE instrument. A known quantity of the sample was placed into a combustion tube at a temperature of 1150 °C. Under these circumstances, CHNS underwent quantitative conversion to their respective gases, namely CO_2, H_2O, NO_X, and SO_X. This conversion occurred during sample combustion at 850°C in an oxygen-rich environment. The resulting gases were then directed into the reduction tube via a U-tube, where impurities such as excess oxides and halides were eliminated using copper and silver metals. Nitrogen content was directly measured using a TCD detector operating at 240°C. Pure elemental oxide gases were trapped in a specific column and subsequently released at a designated temperature for analysis by the TCD detector, with helium serving as the carrier gas. Verification and calibration were conducted using various standards with different concentrations. Elemental analyses were performed on the VR sample and its fractions of ARA (Aromatic, Resins, and Asphaltene). In this process, samples weighing between 25 to 50mg were prepared with double the quantity of tungsten oxide and then injected directly into the column using an auto sampler. The instrument's operational range spanned from 0 to 100%, with a minimum detection limit of 100ppm.

3.2.3 X-ray diffraction

X-ray Diffraction (XRD) is a widely applied analytical technique for investigating the crystalline structure of materials. When X-rays are directed at a sample, they interact with

the atomic planes and are diffracted according to Bragg's law, producing a diffraction pattern that reflects the material's atomic arrangement and long-range order [49]. By analyzing these diffraction patterns, researchers can obtain detailed information about crystal phases, lattice parameters, interlayer spacing, crystallite size, and the degree of crystallinity [50].

XRD has broad applications across disciplines such as materials science, solid-state chemistry, geology, and nanotechnology, where it serves as a fundamental tool for structural characterization [51]. In the present study, XRD measurements were performed using Panalytical's X'Pert Pro diffractometer, equipped with Cu Kα radiation (λ = 1.5406 Å) and a nickel beta filter. The powdered carbon-based samples (particle size below 200 mesh) were analyzed under a scanning speed of 5°/min, ensuring sufficient resolution and signal-to-noise ratio.

Importantly, XRD plays a critical role in the characterization of carbon-based materials, as it provides direct evidence of structural transformations such as graphitization, ordering of graphitic layers, and reduction in graphene oxide systems [42]. For example, the appearance and sharpening of the (002) peak at ~26° 2θ is typically associated with the formation of graphitic structures, while peak shifts or broadening can indicate defects, disorder, or incomplete reduction processes [53].

3.2.4 Thermogravimetric Analysis

Thermogravimetric Analysis (TGA) is a thermal analysis technique used to measure mass changes in a material as a function of temperature or time. It is widely applied in petrochemicals, polymers, pharmaceuticals, and material science to study thermal stability, composition, and decomposition behavior of substances (Jara et al., 2020).

Figure 3.3: TGA Instrumentation

TGA measures the weight loss of a sample as it is heated under a controlled temperature ramp in an inert (e.g., nitrogen) or oxidative (e.g., air) atmosphere.

Steps involved in TGA measurement

1. Sample is heated at a controlled rate (e.g., 10°C/min).
2. Mass loss occurs due to evaporation, decomposition, or oxidation.
3. A highly sensitive balance records weight change.
4. The data is plotted as weight (%) vs. temperature (°C).

Typical Reactions Observed in TGA:

- Moisture Loss: (e.g., Evaporation of water below 150°C)
- Polymer Decomposition: (Breakdown of organic materials at 300-600°C)
- Oxidation & Ash Formation: (Final weight after complete combustion)

Thermal stability investigation of carbon samples was done by using TA Instruments Q500 thermogravimetric analyzer. Samples were analyzed in the temperature range from 20 to 950℃ with a heating rate 10℃/min under atmosphere. 10 mg each sample was taken in the crucible and placed in the instruments.

3.2.5 Raman Spectroscopy

Raman Spectroscopy is a powerful and non-destructive analytical technique that provides insights into the molecular vibrations, crystal structures, and chemical composition of materials. It is based on the principle of inelastic scattering of monochromatic light (usually from a laser source), a phenomenon known as Raman scattering [54]. When laser light interacts with molecular bonds, a fraction of the scattered light experiences an energy shift, producing a unique spectral fingerprint characteristic of the material [55].

This technique is particularly valuable for the characterization of carbon-based materials, such as graphite, graphene, graphene oxide, and carbon nanotubes, because the Raman spectra reveal crucial information about structural defects, crystallinity, disorder, and functional groups [56]. The most prominent features in carbon Raman spectra are the G band (~1580 cm^{-1}), which corresponds to the in-plane stretching of sp^2-bonded carbon atoms, and the D band (~1350 cm^{-1}), which is associated with structural defects, edges, and disorder in the carbon lattice [57]. The 2D band (~2700 cm^{-1}) provides further insights into the degree of graphitization and the number of graphene layers [58].

In this study, Raman spectra were recorded using a Confocal Raman Microscope (LabRAM HR Evolution, HORIBA Scientific) with a 532 nm laser excitation source, which is well-suited for probing the vibrational modes of sp^2 carbon systems. These spectra provided essential information on the graphitization degree, defect density, and structural transformations in the carbon-based samples under investigation. The ratio of the D to G band intensities (I_D/I_G) was particularly analyzed to assess the defect concentration and ordering within the samples [57, 58].

3.3. Results & Discussion

The heat treatment of ARA fractions were carried out in different stages. The products obtained at various stages of heat treatment of ARA fraction were referred as green (stage I), calcined (stage II) and graphitized carbon (stage III). In order to obtain green coke, the ARA fraction was used as raw material. Table 3.5 shows the yield of carbon at different stages of pyrolysis. The highest yield of green carbon for ARA fractions was noticed for

EHCO, except for resin fractions where LCO has more yield. However, the lowest yield of green carbon for ARA fractions was from MCO. The yield of green carbon was in the range of 15.4-23.3, 31.4-41.5 and 52-65 for aromatic, resin and asphaltene fractions. The yield of calcined carbon denotes more conversion has taken place for aromatic and resin fraction when compared to asphaltene. The yield of calcined carbon did not show much variation among ARA fraction and is in the range of 71.5-85. Moreover, the yield of graphitized carbon for all ARA fraction are above 90. Almost complete conversion has taken place for aromatic (EHCO) and asphaltene (HCO) which is 99.3 and 99.5.

SAMPLE	AROMATIC			RESIN			ASPHALTENE		
	LCO	HCO	EHCO	LCO	HCO	EHCO	LCO	HCO	EHCO
Green Carbon	21.9	15.4	23.3	41.5	31.4	38.4	62.3	52.0	65.0
Calcined Carbon	85.0	79.4	82.4	83.9	82.4	80.4	75.7	75.6	71.5
Graphitized carbon	96.2	96.0	99.3	92.5	95.8	97.7	94.5	99.5	98.0

Table 3.5: Yield of carbon at different stages of pyrolysis.

3.3.1 Elemental analysis (CHNSO) of different stages of carbon samples

The effect of pyrolysis temperature on elemental content is presented in Table 3.6. Table 3.6 shows that carbon content increases on calcination and graphitization of green carbon. At the same time, as expected there was a progressive decrease of hydrogen, nitrogen, sulphur and oxygen with calcination and graphitization process corresponding to an increase of volatile and gases (CO, CO2, NO2, CH4) loss. The decrease of oxygen is anticipated to increase the sample basic nature. Hence, the increased C/H and C/O ratios are indicative of dehydrogenative polymerization and dehydrative polycondensation during heat treatment. Further, the relatively high quantities of heteroatoms in green carbon decreases on calcination and graphitization showing the loss of numerous functional groups. The highest amount of carbon (99.99) in all ARA fractions after graphitization process indicates the complete graphitization.

Origin	Sample	Total Carbon	Total Hydrogen	Total Nitrogen	Total Sulphur	Total Oxygen	Total Heteroatoms
Aromatic LCO	**Green**	89.39	2.43	0.69	5.39	2.10	8.18
	Calcined	98.21	0.07	0.21	1.51	0.00	1.72
	Graphitized	99.99	0.00	0.01	0.00	0.00	0.01
Aromatic HCO	**Green**	88.59	2.68	1.26	5.40	2.07	8.73
	Calcined	97.94	0.03	0.31	1.72	0.00	2.03
	Graphitized	99.99	0.00	0.01	0.00	0.00	0.01
Aromatic EHCO	**Green**	91.02	2.82	1.45	3.60	1.11	6.16
	Calcined	94.79	0.03	0.32	2.31	2.55	5.18
	Graphitized	99.99	0.00	0.01	0.00	0.00	0.01
Resin LCO	**Green**	88.17	2.10	1.18	6.69	1.86	9.73
	Calcined	96.82	0.04	0.34	2.81	0.00	3.14
	Graphitized	99.99	0.00	0.01	0.00	0.00	0.01
Resin HCO	**Green**	88.36	2.55	1.98	4.03	3.08	9.09
	Calcined	96.38	0.03	0.51	2.74	0.35	3.60
	Graphitized	99.99	0.00	0.01	0.00	0.00	0.01
Resin EHCO	**Green**	88.36	2.55	1.98	4.03	3.08	9.09
	Calcined	96.38	0.03	0.51	2.74	0.35	3.60
	Graphitized	99.99	0.00	0.01	0.00	0.00	0.01
Asphaltene LCO	**Green**	87.60	2.01	1.57	7.02	1.80	10.39
	Calcined	95.47	0.04	0.19	2.05	2.25	4.49
	Graphitized	99.99	0.00	0.01	0.00	0.00	0.01
Asphaltene HCO	**Green**	82.27	1.77	2.50	7.83	5.64	15.97
	Calcined	94.61	0.02	0.35	3.01	2.02	5.38
	Graphitized	99.99	0.00	0.01	0.00	0.00	0.01
Asphaltene EHCO	**Green**	87.19	2.16	2.36	4.69	3.60	10.65
	Calcined	94.93	0.01	0.43	3.48	1.15	5.06
	Graphitized	99.99	0.00	0.01	0.00	0.00	0.01

Table 3.6: Elemental analysis (CHNSO) of different stages of carbon samples.

3.3.2 XRD

The XRD patterns of the green, calcined and graphitized origin based aromatic fraction are shown in fig.4.1. A difference in XRD pattern was noticed, green carbon exhibited prominent peaks at approximately 2 theta=25.46º and remaining peaks with relatively weak intensity broad peaks emerging at around 2 theta= 43.24º. These correspond to the (002) and (004) reflection planes of reduced graphene oxide, respectively. On calcination, the XRD pattern shows slight shift towards higher angle along with intensity growth indicating graphitization. The appearance of asymmetric peak existence of both reduced graphene oxide and graphitic carbon. Further on graphitization the peak turns completely symmetric with a sharp peak representing the presence of only graphite. Moreover, a small peak at 2 theta =54.56º belonging to graphite confirms the complete conversion of reduced graphene oxide to graphite. The HCO and EHCO fractions fig. 3.2 & 3.3 for green, calcined and graphitized represent the same behavior comparative to aromatic fraction as shown in fig. 3.1, except for a small change. In the case of calcined HCO, there are additional sharp peaks at 2 theta =21.86º, 31.54º and 36.25º. Even for resin and asphaltene fraction, the XRD patterns show the same behavior as observed in aromatic fraction for all green, calcined and graphitized processes.

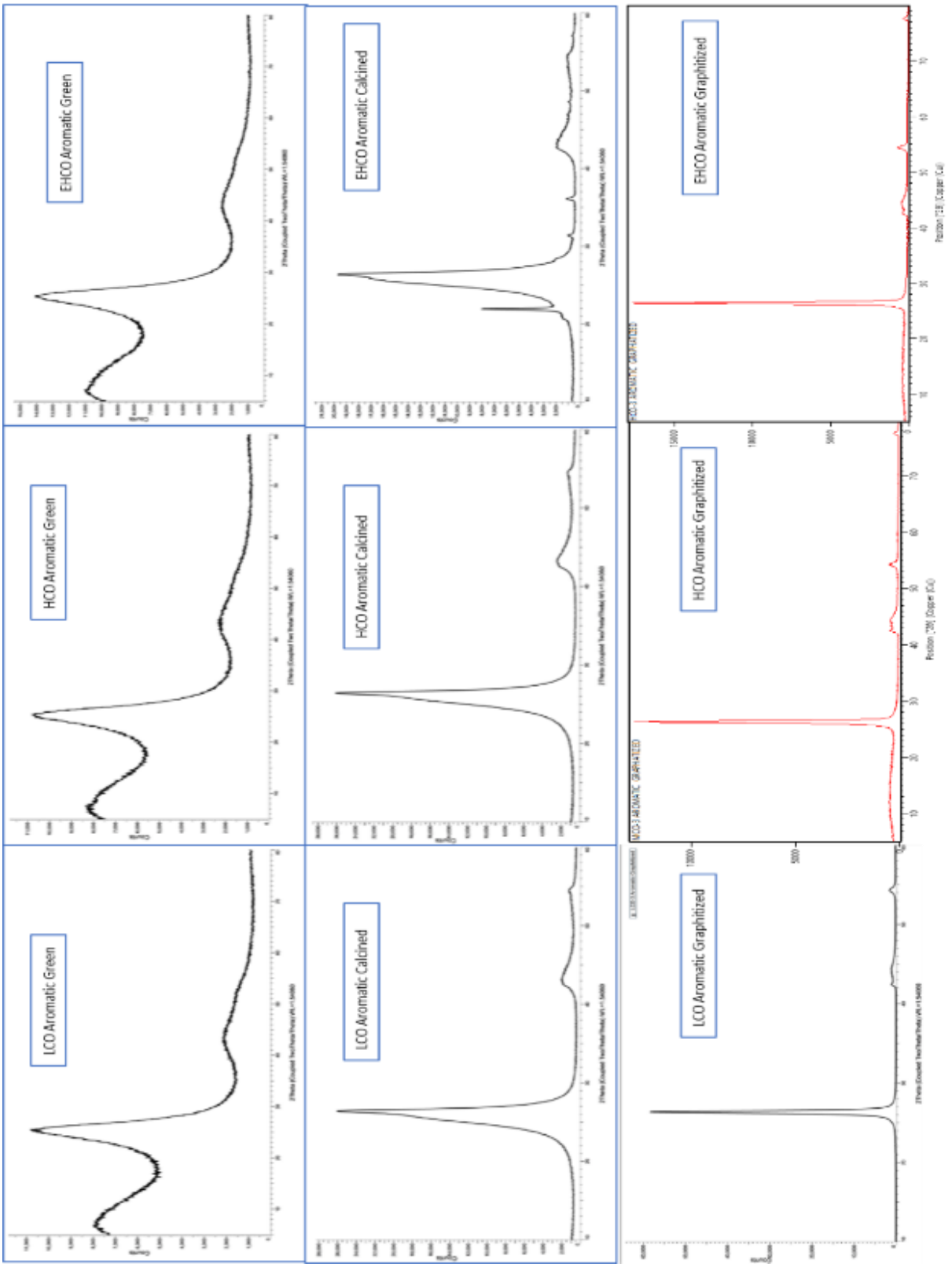

Figure 3.3: XRD pattern of green, calcined and graphitized samples from aromatics.

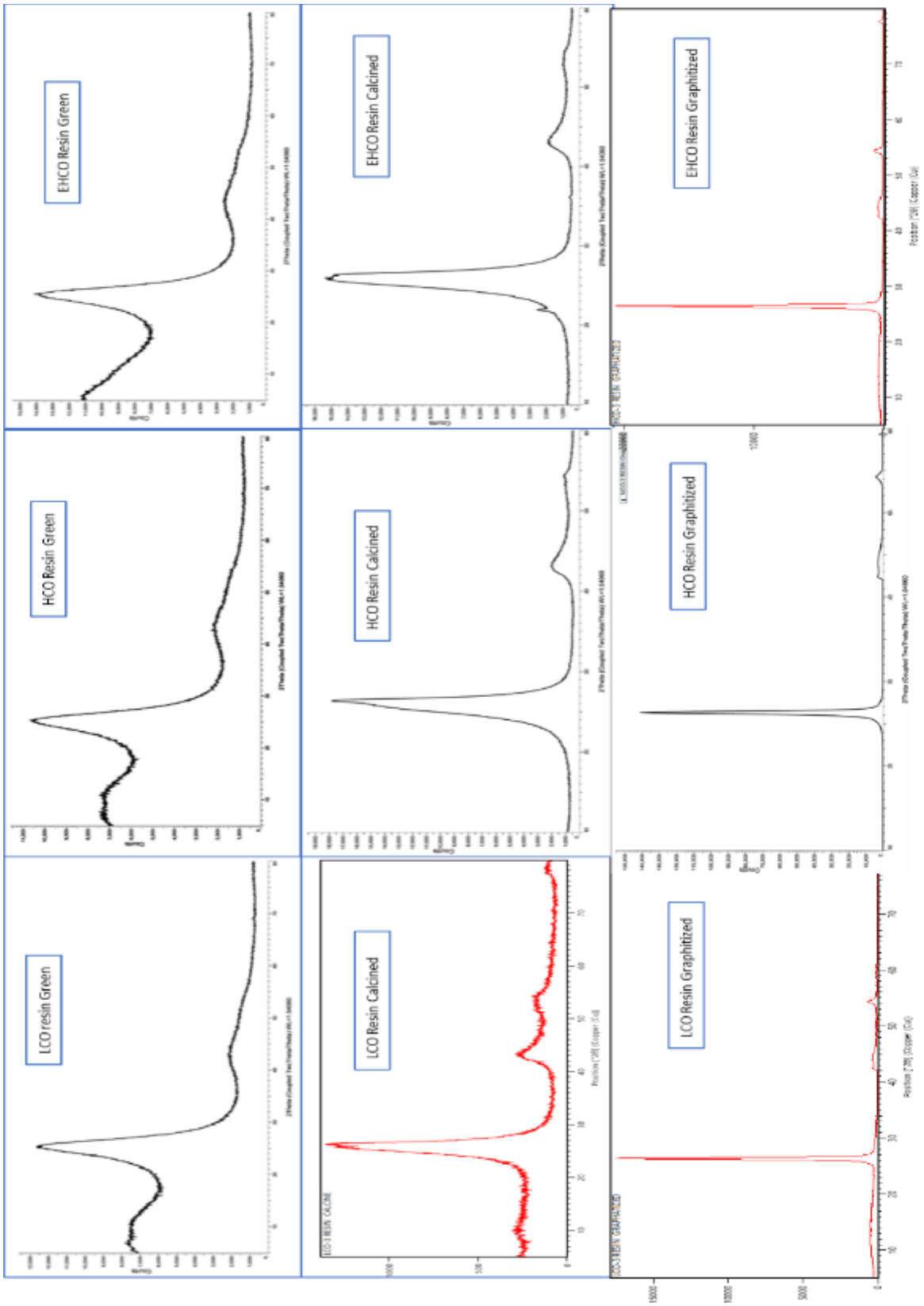

Figure 3.4: XRD pattern of green, calcined and graphitized samples from resins.

Figure 3.5: XRD pattern of green, calcined and graphitized samples from asphaltenes.

The interlayer spacing obtained from the XRD patterns are given in table 3.3. The interlayer spacing of green carbon was around the range 3.505-3.538 Å, this confirms the presence of reduced graphene oxide. Moreover, the interlayer spacing of calcined and graphitized carbon decreases to around 3.36 Å indicating the transformation of rGO to graphite. In addition the crystallite size L_a and L_c were calculated to assess the average size of the carbon atoms. In the green sample, the L_c and L_a were in the range 19.90-24 Å and 16.90-25.30 Å which shows a notable decrease in calcination indicating the increase of defects in the structure. Further, with graphitization there was once again a remarkable increase in Lc and La values suggesting the increase of order with the transformation to graphite structure. There was not any distinguishable difference in interplanar spacing and crystallite size with origin as well ARA fraction.

Sample	**Origin**	**AROMATIC**			**RESIN**			**ASPHALTENE**		
		d-spacing (A°)	**Lc (A°)**	**La (A°)**	**d-spacing (A°)**	**Lc (A°)**	**La (A°)**	**d-spacing (A°)**	**Lc (A°)**	**La (A°)**
Green	LCO	3.515	21.30	16.90	3.518	22.60	21.90	3.505	22.80	18.10
Calcined		3.380	8.022	4.165	3.386	7.868	4.487	3.47	3.16	3.53
Graphitized		3.382	20.279	43.062	3.379	19.673	43.004	3.372	19.23	34.59
Green	HCO	3.528	20.70	19.70	3.538	20.90	24.10	3.524	19.90	25.30
Calcined		3.377	8.290	4.332	3.381	6.924	3.865	3.387	6.09	3.89
Graphitized		3.387	17.814	45.672	3.387	18.744	39.774	3.371	16.75	34.89
Green	EHCO	3.522	21.20	19.80	3.513	21.40	20.80	3.507	24.00	21.80
Calcined		3.380	7.581	3.541	3.392	5.432	4.115	3.389	5.87	3.54
Graphitized		3.380	24.579	36.645	3.362	20.712	33.085	3.371	18.49	38.04

Table 3.7: XRD analysis of Green, Calcined and Graphitized samples obtained from different origin

3.3.3 Raman spectroscopy:

The presence of reduced graphene oxide and graphite in the samples has been further supported by Raman spectroscopy. In the recent years, pyrolysis of petroleum vacuum residue is procuring significant recognition with raising awareness on sustainability, the

transformation and nature of carbonaceous substances were analyzed in depth with the aid of Raman spectroscopy (Zhang et al., 2017). As shown in fig.3.6, the Raman spectrum of rGO exhibits strong lines at 1355 cm-1 and 1575 cm^{-1}, which are designated to the D band and G band, correspondingly. These peaks grow sharp and intense on calcination, indicating the increase of rGO amount. Additionally, a broad peak evolves around 2500 cm^{-1} denoting the coexistence of the graphite phase. With the further increase in temperature during the graphitization process, the Raman spectrum exhibits defect (D) and graphitic (G) bands at 1354 and 1584 cm-1 and an overtone 2D band at about 2716 cm-1, reflecting the transformation of rGO to graphite. The Raman spectra of other samples particularly origin based along with ARA fraction reveal similar patterns.

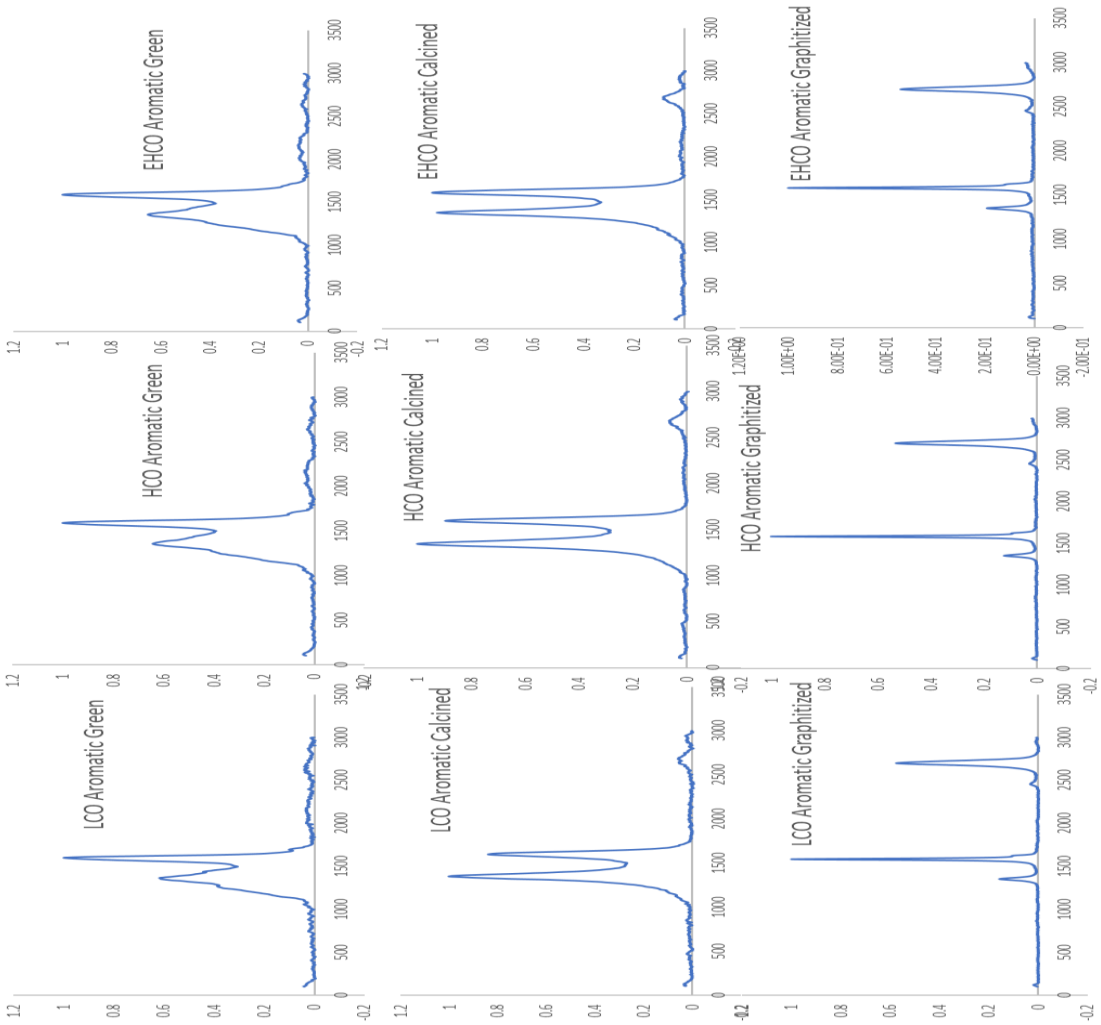

Figure 3.6: Raman spectra of green, calcined and graphitized carbon of origin-based aromatics.

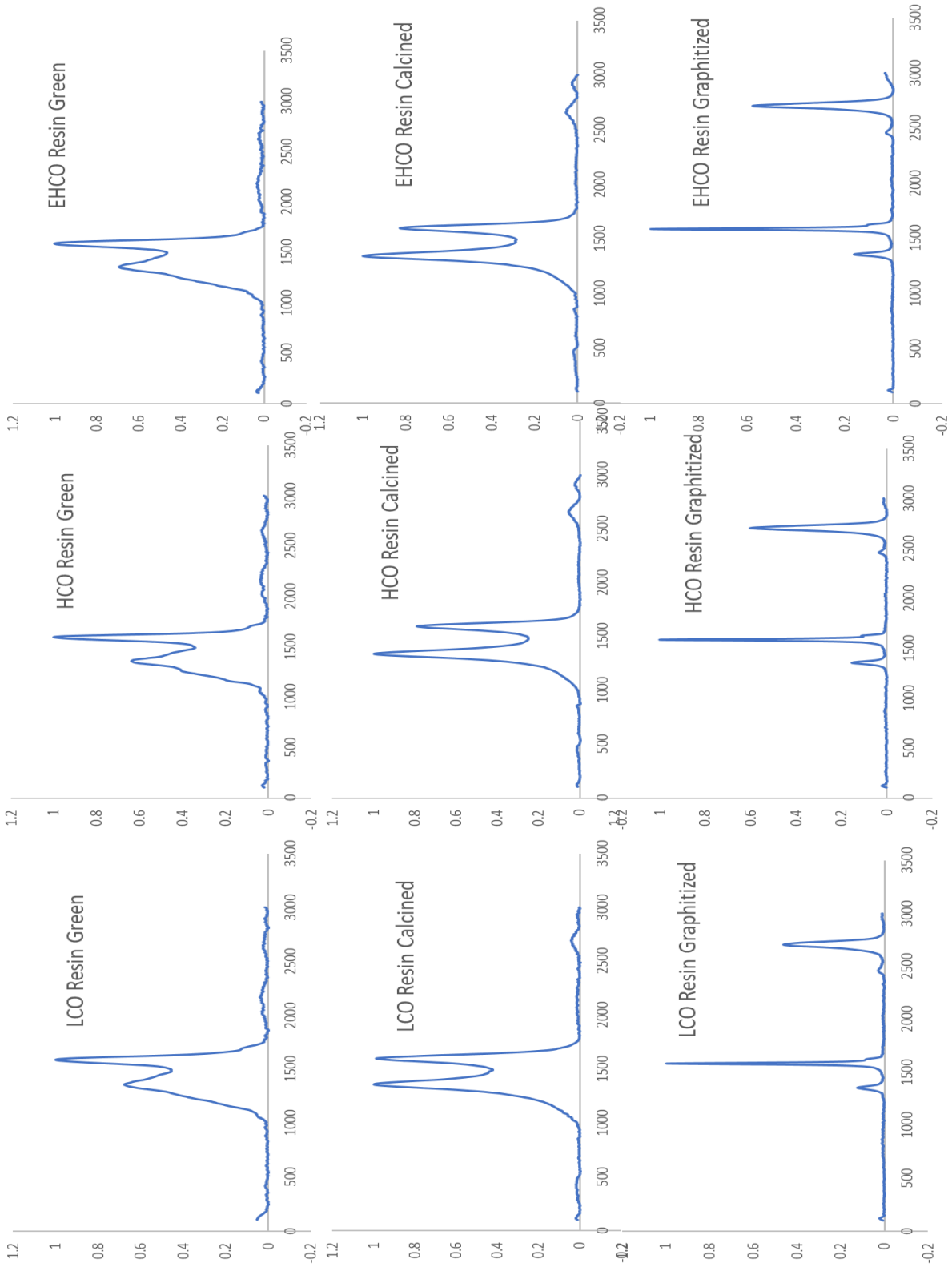

Figure 3.7: Raman spectra of green, calcined and graphitized carbon of origin-based resins.

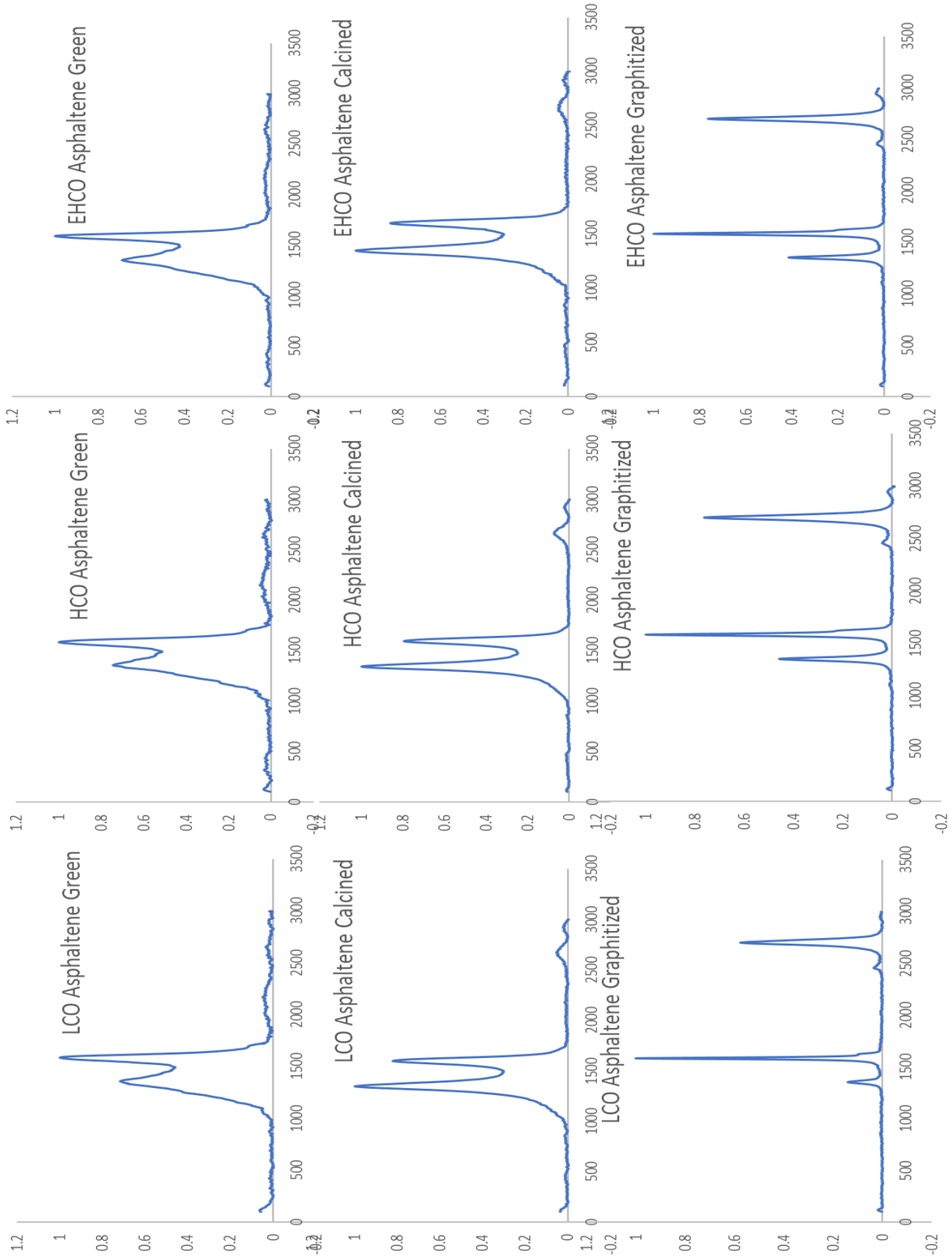

Figure 3.8: Raman spectra of green, calcined and graphitized carbon of origin-based asphaltenes.

The ratio of I_D/I_G estimated for the studied specimens are denoted in Table 3.8. While the G-band is produced by the C-C stretching and exists in all carbon structures, the D-band evolves from the breathing mode of aromatic rings (Scardaci et al., 2021). The D-band indicates the disorder in formed rGO. The intensity ratio of the D and G band (ID/IG) may thus be an indirect assessment of the disorder within the sample. The ID/IG values for the ARA fraction of the green sample were in the range 0.6164-0.6890, representing disordered structure. Slightly higher I_D/I_G values were noted for graphitized resin as well green and calcined asphaltene. The I_D/I_G value once again increases which later decreases with increase in temperature, indicating the changes in rGO to graphite.

Sample	Origin	AROMATIC		RESIN		ASPHALTENE	
		ID/IG	La (nm)	ID/IG	La (nm)	ID/IG	La (nm)
Green	LCO	0.6164	31.19	0.6773	28.39	0.7175	26.79
	MCO	0.6424	29.92	0.6372	30.17	0.7454	25.79
	HCO	0.624	29.47	0.922	27.77	0.689	27.9
Calcined	LCO	1.1925	16.12	1.0112	19.01	1.2171	15.8
	MCO	1.1169	17.21	1.2641	15.21	1.2571	15.29
	HCO	0.9812	19.59	1.2083	15.91	1.1948	16.09
Graphitized	LCO	0.1581	121.61	0.1241	154.95	0.1401	137.23
	MCO	0.1234	155.79	0.1552	123.84	0.458	41.98
	HCO	0.1902	101.07	0.1619	118.77	0.4149	46.34

Table 3.8: Raman analysis of Green, Calcined and Graphitized samples obtained from different origin

3.3.4 TGA

Fig 3.9 shows the thermogravimetric analysis of green, calcined and graphitized samples of ARA fractions. The TGA curve of the green aromatic fraction represented three decomposition stages. However, the overall weight loss was only 7%. The first weight loss

step started at about 27.8 ºC, was related to adsorbed moisture and impurities. While the second weight loss step initiated at about 554.28 ºC may be attributed to the reaction of carbon with oxygen leading to the release of CO2 (Jara et al., 2020). The third weight loss step at around 727 ºC may be to the sublimation of carbon backbone (Alam et al., 2017). The TGA curve of calcined and graphitized aromatic fraction shows negligible weight loss indicating the thermal stability of the formed graphite. The characteristics were identical for resin and asphaltene fractions.

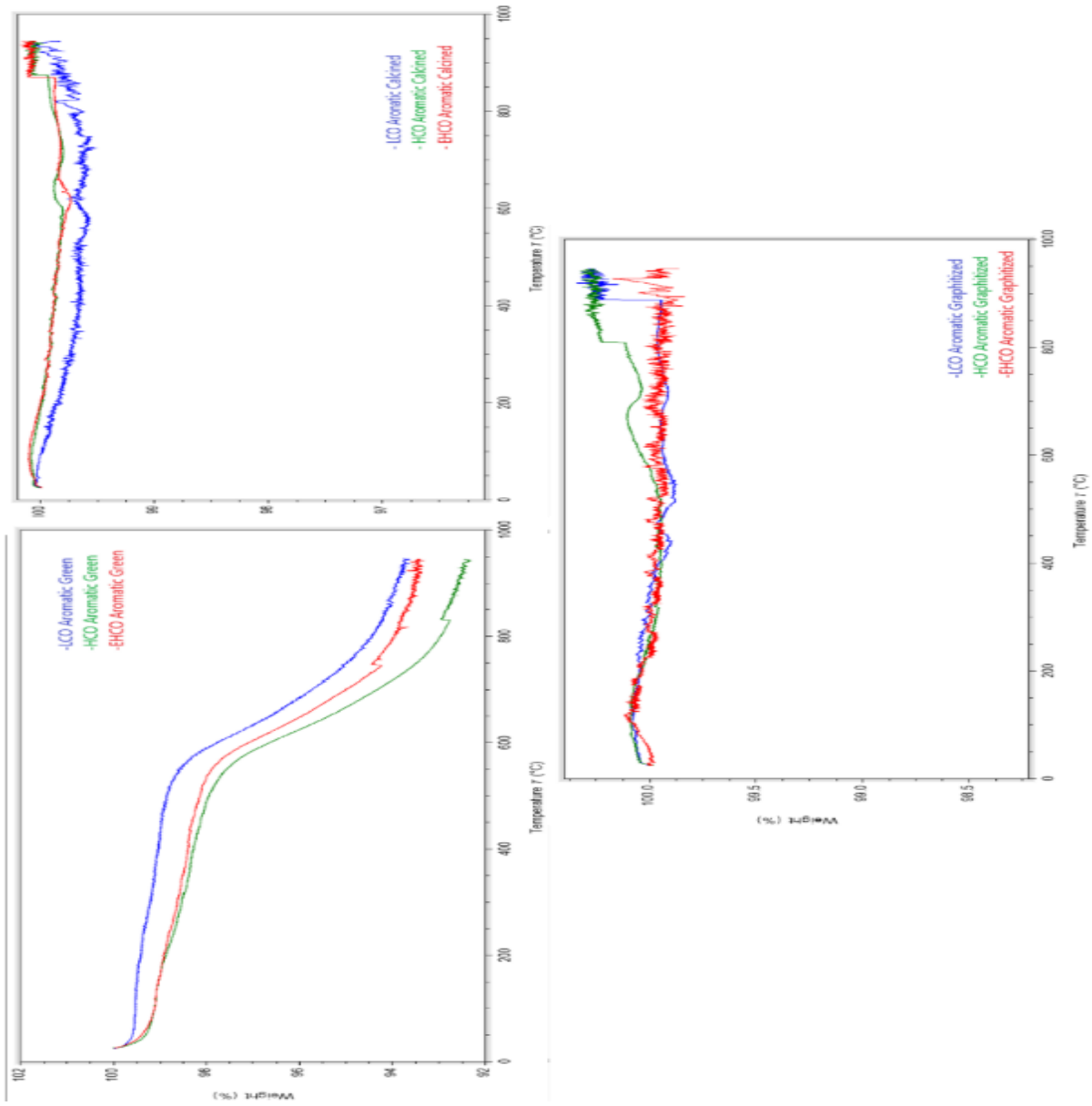

Figure 3.9: TGA analysis of green, calcined and graphitized carbon from origin-based aromatic fractions.

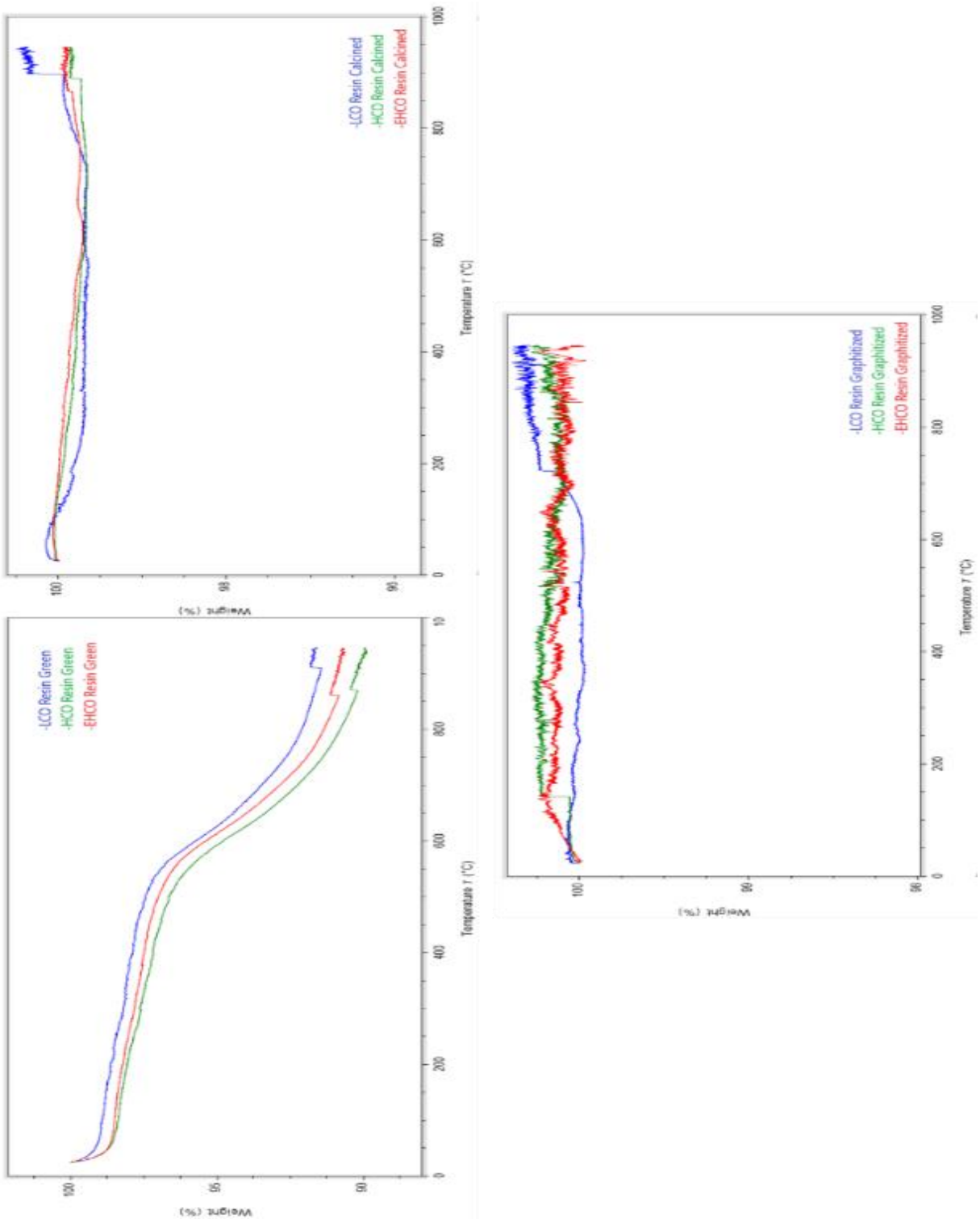

Figure 3.10: TGA analysis of green, calcined and graphitized carbon from origin-based resins fractions

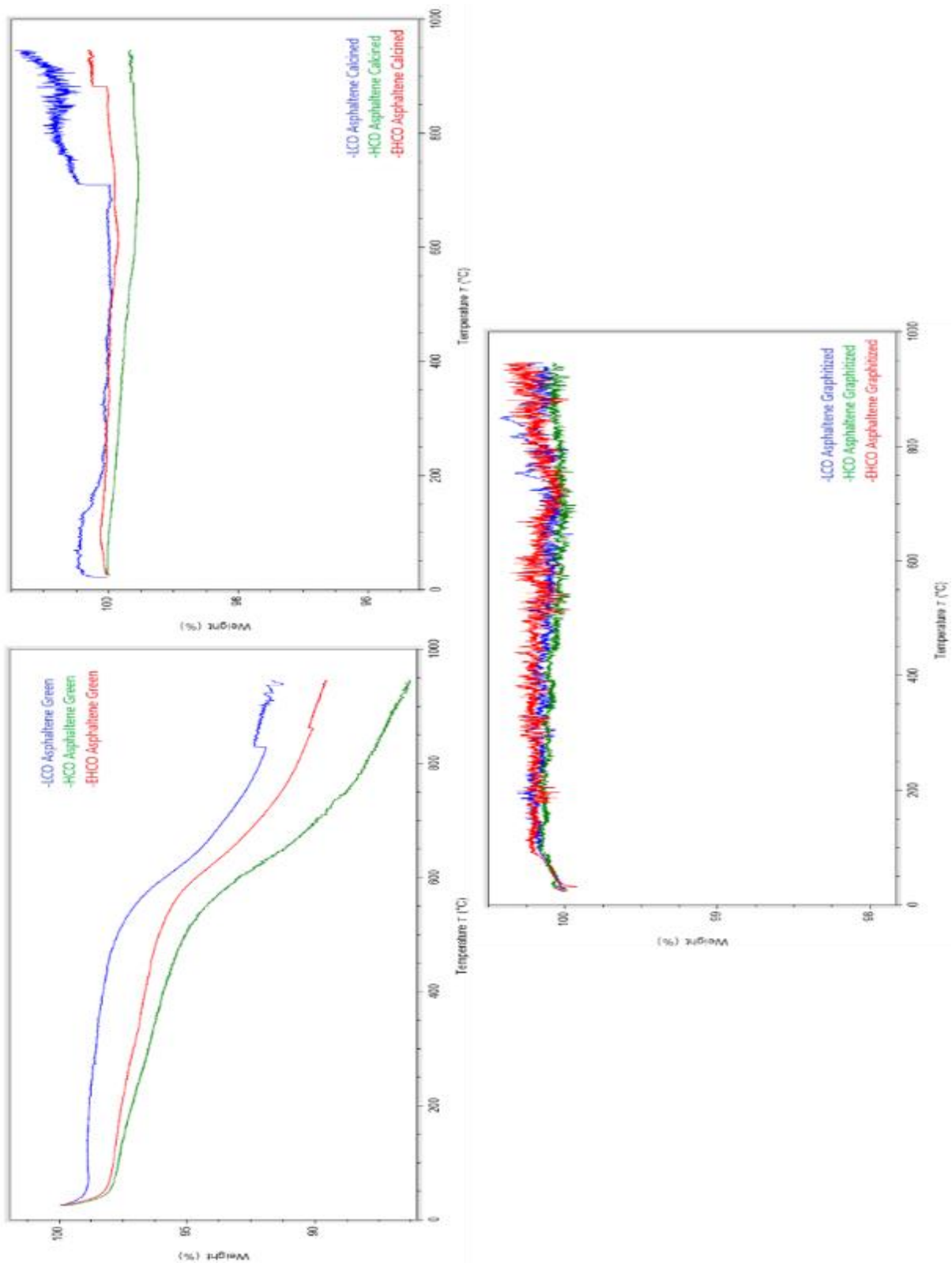

Figure 3.11: TGA analysis of green, calcined and graphitized carbon from origin-based asphaltenes fractions.

Conclusion

This study successfully demonstrated the synthesis of carbon materials from various petroleum fractions (aromatic, resin, and asphaltene) through a three-stage heat treatment process: green, calcined, and graphitized. The results consistently show that pyrolysis effectively converts these complex hydrocarbon mixtures into high-purity carbon, with the final graphitized product exhibiting properties characteristic of graphite.

Key Findings and Summary of Results

- **Pyrolysis Yields and Carbon Purity:** The heat treatment process systematically increased the carbon yield and purity. While the green carbon yield varied significantly based on the fraction (aromatics, resins, asphaltenes), with asphaltenes showing the highest yields, the graphitized carbon yield consistently exceeded 90% for all fractions, indicating near-complete conversion. The elemental analysis confirmed this, as carbon content increased to 99.99% in the graphitized stage, with a corresponding progressive decrease in hydrogen, nitrogen, sulfur, and oxygen.
- **Structural Transformation (XRD and Raman Spectroscopy):** The structural evolution from an amorphous to a highly ordered graphitic structure was clearly tracked using XRD and Raman spectroscopy.
    - **XRD analysis** showed a transition from the broad peaks of reduced graphene oxide (rGO) in the green carbon to the sharp, symmetric peaks of graphite in the graphitized samples. The decrease in interlayer spacing (d-spacing) from ~3.5 A˚ to ~3.37 A˚ and the significant increase in crystallite size (Lc and La) confirm the formation of a well-ordered graphitic structure.
    - **Raman spectroscopy** further supported this transformation. The green samples showed a high ID/IG ratio, indicative of a disordered structure. This ratio initially increased upon calcination, suggesting the formation of more defects, but then dramatically decreased in the graphitized samples, confirming the restoration of structural order as rGO converted to graphite.

- **Thermal Stability (TGA):** The thermal analysis demonstrated the increasing stability of the carbon samples with each heat treatment stage. The green carbon showed multiple stages of weight loss due to the removal of moisture, impurities, and volatile organic compounds. In stark contrast, the calcined and especially the graphitized samples exhibited negligible weight loss, highlighting their high thermal stability—a key property of graphite.

In conclusion, this research confirms that the multi-stage heat treatment of aromatic, resin, and asphaltene fractions from various crude oil sources is a highly effective method for producing high-purity, thermally stable graphitic carbon. The systematic analysis using elemental analysis, XRD, Raman spectroscopy, and TGA provides robust evidence of the progressive conversion from disordered carbonaceous materials to a highly ordered graphitic structure. The final graphitized products, regardless of the initial ARA fraction, show remarkable similarity in their structural and compositional properties, suggesting that this method can be a viable and reliable route for valorising different petroleum fractions into valuable carbon materials. The negligible variations in the final properties among the different fractions imply that the heat treatment process successfully overcomes the initial compositional differences, resulting in a uniform end-product.

References

1. Mochida, I., & Korai, Y. (2000). Chemistry in the conversion of pitch to carbon fiber. *Carbon*, 38(2), 305–328. https://doi.org/10.1016/S0008-6223(99)00120-9
2. Liu, X., Zhang, L., & Li, J. (2015). Preparation of mesophase pitch from petroleum residues: Structure–processing–property correlations. *Fuel Processing Technology*, 134, 46–54. https://doi.org/10.1016/j.fuproc.2015.02.019
3. Yamada, Y., Sato, S., & Ohtani, Y. (1975). Preparation of petroleum-based binder pitches by heat treatment of vacuum residue. *Carbon*, 13(2), 123–129. https://doi.org/10.1016/0008-6223(75)90025-9
4. Zhou, J., Wang, Z., & Zhang, H. (2019). Development of binder pitches from vacuum residue and petroleum fraction oil for high-density graphite blocks. *Journal of Analytical and Applied Pyrolysis*, 141, 104638. https://doi.org/10.1016/j.jaap.2019.104638
5. Derbyshire, F. J., Ouchi, K., & Patrick, J. W. (1991). The formation of anisotropic coke. *Fuel*, 70(4), 549–567. https://doi.org/10.1016/0016-2361(91)90151-I
6. Marsh, H., & Rodríguez-Reinoso, F. (2006). *Activated Carbon*. Elsevier. https://doi.org/10.1016/B978-0-08-044463-5.X5000-7
7. Qian, W., Guo, Y., & Zhang, H. (2003). Structure evolution of petroleum-based needle coke during carbonization. *Carbon*, 41(13), 2561–2566. https://doi.org/10.1016/S0008-6223(03)00306-9
8. Nomura, S., & Mochida, I. (1994). In-situ optical texture observation during mesophase development in heavy oil carbonization. *Fuel*, 73(11), 1761–1766. https://doi.org/10.1016/0016-2361(94)90205-4
9. Endo, M., Kim, C., Nishimura, K., Fujino, T., & Miyashita, K. (2000). Recent development of carbon materials for Li ion batteries. *Carbon*, 38(2), 183–197. https://doi.org/10.1016/S0008-6223(99)00141-6
10. Kelly, B. T. (1981). *Physics of graphite*. Applied Science Publishers.
11. Pierson, H. O. (1993). *Handbook of Carbon, Graphite, Diamonds and Fullerenes: Properties, Processing and Applications*. Noyes Publications.

12. Mochida, I., Korai, Y., Ku, C. H., Watanabe, F., & Sakai, Y. (2000). Chemistry of synthetic graphite. *Carbon*, 38(2), 305–328. https://doi.org/10.1016/S0008-6223(99)00120-9
13. Marsh, H., & Rodríguez-Reinoso, F. (2006). *Activated Carbon*. Elsevier. https://doi.org/10.1016/B978-0-08-044463-5.X5000-7
14. Endo, M., Kim, C., Nishimura, K., Fujino, T., & Miyashita, K. (2000). Recent development of carbon materials for Li-ion batteries. *Carbon*, 38(2), 183–197. https://doi.org/10.1016/S0008-6223(99)00141-6
15. Syrett, B. C., & Starkey, D. (2011). Natural graphite. In K. J. R. Roskill (Ed.), *The Economics of Natural Graphite*. Roskill Information Services.
16. Jara, A. D., Betemariam, A., Woldetinsae, G., & Kim, J. Y. (2019). Purification, application and current market trend of natural graphite: A review. *International Journal of Mining Science and Technology*, 29(5), 671–689. https://doi.org/10.1016/j.ijmst.2019.07.003
17. Wang, M., Li, J., & Zhang, L. (2016). Microstructure and electrochemical performance of synthetic graphite. *Electrochimica Acta*, 215, 667–674. https://doi.org/10.1016/j.electacta.2016.08.097
18. Lu, X., & Chung, D. D. L. (2001). Structure of natural graphite and its electrical properties. *Carbon*, 39(7), 1111–1115. https://doi.org/10.1016/S0008-6223(00)00238-0
19. Krishnan, S. (2017). Crystallite size distribution and anisotropy in natural graphite deposits. *Journal of Materials Science*, 52(8), 4725–4737. https://doi.org/10.1007/s10853-016-0784-5
20. Zhao, W., Ci, L., & Zhu, H. (2010). Performance comparison of natural and synthetic graphite for lithium-ion batteries. *Electrochimica Acta*, 55(22), 6802–6808. https://doi.org/10.1016/j.electacta.2010.05.091
21. Kelly, B. T. (1981). *Physics of Graphite*. Applied Science Publishers.
22. Kamitakahara, W. A., & Slack, G. A. (1982). Density and porosity of natural graphite. *Journal of Materials Science*, 17(3), 601–606. https://doi.org/10.1007/BF00591412

23. Mochida, I., & Yoon, S. H. (2012). Synthetic graphite production from petroleum and coal-tar pitch. *Carbon Letters*, 13(1), 1–10. https://doi.org/10.5714/CL.2012.13.1.001
24. Inagaki, M., Kang, F., & Toyoda, M. (2014). *Graphene, Graphite, and Carbon Nanotubes: Handbook of Synthetic Graphite*. Elsevier. https://doi.org/10.1016/C2012-0-07128-6
25. Dresselhaus, M. S., & Terrones, M. (2012). Carbon-based nanomaterials: Natural versus synthetic. *Philosophical Transactions of the Royal Society A: Mathematical, Physical and Engineering Sciences*, 370(1972), 2829–2845. https://doi.org/10.1098/rsta.2011.0340
26. Speight, J. G. (2014). *The Chemistry and Technology of Petroleum* (5th ed.). CRC Press.
27. Mochida, I., & Yoon, S. H. (2012). Synthetic graphite production from petroleum residues. *Carbon Letters*, 13(1), 1–10. https://doi.org/10.5714/CL.2012.13.1.001
28. Ancheyta, J., & Speight, J. G. (2007). *Hydroprocessing of Heavy Oils and Residua*. CRC Press.
29. Speight, J. G. (1999). *The Desulfurization of Heavy Oils and Residua* (2nd ed.). Marcel Dekker.
30. Ali, M. F., & Abbas, S. (2006). *Handbook of Oil Refining Processes*. CRC Press.
31. Rana, M. S., Samano, V., Ancheyta, J., & Diaz, J. A. I. (2007). A review of recent advances on process technologies for upgrading of heavy oils and residua. *Fuel*, 86(9), 1216–1231. https://doi.org/10.1016/j.fuel.2006.08.004
32. Ancheyta, J., Trejo, F., & Rana, M. S. (2009). *Asphaltenes: Chemical Transformation during Hydroprocessing of Heavy Oils*. CRC Press.
33. Speight, J. G. (2004). *Petroleum Asphaltenes: Part, Whole, or More than the Sum?* Springer. https://doi.org/10.1007/978-1-4615-0579-4
34. Mochida, I., Korai, Y., Ku, C. H., Watanabe, F., & Sakai, Y. (2000). Chemistry in the conversion of pitch to carbon fiber. *Carbon*, 38(2), 305–328. https://doi.org/10.1016/S0008-6223(99)00120-9

35. Vazquez, D., Mansoori, G. A., & Shariaty-Niassar, M. (2009). Physicochemical characterization of petroleum heavy fractions. *Journal of Petroleum Science and Engineering*, 65(1–2), 93–98. https://doi.org/10.1016/j.petrol.2008.12.029
36. EA. *Global EV Outlook 2023*. International Energy Agency, 2023.
37. Choi, N. S., et al. *Challenges facing lithium batteries and electrical double-layer capacitors*. Angewandte Chemie International Edition, 51, 9994–10024 (2012).
38. Zhang, S. S. *A review on electrolyte additives for lithium-ion batteries*. Journal of Power Sources, 162, 1379–1394 (2006).
39. Zheng, H., et al. *Electrochemical performance of synthetic graphite as anode material in Li-ion batteries*. Journal of The Electrochemical Society, 160, A2290–A2294 (2013).
40. Zhang, S. S. A review on electrolyte additives for lithium-ion batteries. Journal of Power Sources, 162, 1379–1394 (2006).
41. Zheng, H., et al. Electrochemical performance of synthetic graphite as anode material in Li-ion batteries. Journal of The Electrochemical Society, 160, A2290–A2294 (2013).
42. Grand View Research. (2023). *Synthetic Graphite Market Size, Share & Trends Report, 2023–2034*. Retrieved from https://www.grandviewresearch.com
43. Chen, M., Ma, X., Chen, B., & Zhou, T. (2022). Recovery of anode graphite from spent lithium-ion batteries: Challenges and opportunities. *Journal of Hazardous Materials, 426*, 127870. https://doi.org/10.1016/j.jhazmat.2021.127870
44. Fortune Business Insights. (2024). *Synthetic Graphite Market Report: Trends and Forecast, 2024–2032*. Retrieved from https://www.fortunebusinessinsights.com
45. Lee, S. Y., Kim, H. J., & Park, J. Y. (2021). Biochar-derived graphite as a sustainable anode material for lithium-ion batteries. *Carbon, 183*, 236–246. https://doi.org/10.1016/j.carbon.2021.07.021
46. Olivetti, E. A., Ceder, G., Gaustad, G. G., & Fu, X. (2017). Lithium-ion battery supply chain considerations: Analysis of potential bottlenecks in critical metals. *Joule, 1*(2), 229–243. https://doi.org/10.1016/j.joule.2017.08.019

47. Xu, C., Dai, Q., Gaines, L., Hu, M., Tukker, A., & Steubing, B. (2020). Future material demand for automotive lithium-based batteries. *Nature Communications, 11*, 4906. https://doi.org/10.1038/s41467-020-18424-3
48. Doughty, H., & Wang, J. (2023). Renewable biomass-derived carbon materials for energy storage applications. *Advanced Energy Materials, 13*(22), 2203790. https://doi.org/10.1002/aenm.202203790
49. Epp, J. (2016). X-ray diffraction (XRD) techniques for materials characterization. *Materials Characterization, 117*, 1–25. https://doi.org/10.1016/j.matchar.2016.04.008
50. Khan, M., Khan, A., & Kim, Y. (2020). X-ray diffraction techniques for structural analysis of nanomaterials. *Crystals, 10*(6), 437. https://doi.org/10.3390/cryst10060437
51. Cullity, B. D., & Stock, S. R. (2014). *Elements of X-ray diffraction* (3rd ed.). Pearson.
52. Ferrari, A. C., & Basko, D. M. (2013). Raman spectroscopy as a versatile tool for studying the properties of graphene. *Nature Nanotechnology, 8*(4), 235–246. https://doi.org/10.1038/nnano.2013.46
53. Fang, M., Wang, K., Lu, H., Yang, Y., & Nutt, S. (2009). Covalent polymer functionalization of graphene nanosheets and mechanical properties of composites. *Journal of Materials Chemistry, 19*(38), 7098–7105. https://doi.org/10.1039/B908220D
54. Long, D. A. (2002). *The Raman effect: A unified treatment of the theory of Raman scattering by molecules*. John Wiley & Sons.
55. Smith, E., & Dent, G. (2019). *Modern Raman spectroscopy: A practical approach* (2nd ed.). John Wiley & Sons.
56. Ferrari, A. C., & Robertson, J. (2000). Interpretation of Raman spectra of disordered and amorphous carbon. *Physical Review B, 61*(20), 14095–14107. https://doi.org/10.1103/PhysRevB.61.14095
57. Tuinstra, F., & Koenig, J. L. (1970). Raman spectrum of graphite. *The Journal of Chemical Physics, 53*(3), 1126–1130. https://doi.org/10.1063/1.1674108

58. Ferrari, A. C., & Basko, D. M. (2013). Raman spectroscopy as a versatile tool for studying the properties of graphene. *Nature Nanotechnology, 8*(4), 235–246. https://doi.org/10.1038/nnano.2013.46